Evidence and control of unintentional As-rich shells in GaAs 1– x P x nanowires

Romaric de Lépinau, Andrea Scaccabarozzi, Gilles Patriarche, Laurent Travers, Stéphane Collin, Andrea Cattoni, Fabrice Oehler

Evidence and control of unintentional As-rich shells in $GaAs_{1-x}P_x$ nanowires

Romaric de Lépinau[1,2], Andrea Scaccabarozzi[2], Gilles Patriarche[2], Laurent Travers[2], Stéphane Collin[1,2], Andrea Cattoni[1,2], Fabrice Oehler[2]

[1]*IPVF, Institut Photovoltaïque d'Île-de-France, 91120 Palaiseau, France*
[2] *C2N, Centre de Nanosciences et de Nanotechnologies, UMR 9001 CNRS, Univ. Paris Sud, Univ. Paris-Saclay, 91120 Palaiseau, France*

1 Abstract

We report on the detailed composition of ternary GaAsP nanowires (NWs) grown using self-catalyzed vapor-liquid-solid (VLS) growth by molecular beam epitaxy (MBE). We evidence the formation of an unintentional shell, which enlarges by vapor-solid (VS) growth concurrently to the main VLS-grown core. The NW core and unintentional shell have typically different chemical compositions if no effort is made to adjust the growth conditions. The compositions can be made equal by changing the substrate temperature and P:As flux ratio in the vapor phase. In all cases, we still observe the existence of a P-rich interface between the GaAsP NW core and the unintentional shell, even if favorable growth conditions are used.

2 Introduction

Today's photovoltaic market is dominated by Si-wafer based solar cells with 95% share of production [1]. The record efficiency for this technology is 26.7% [2], approaching the maximum theoretical efficiency of 29.4% [3]. Tandem solar cells combining a top III-V semiconductor top cell with a Si bottom solar cell are currently one of the most studied routes to exceed 30% efficiency. Direct epitaxy of III-V on Si using a transition layer to accommodate the different lattice constants remains a challenge [4]. Direct bonding of the III-V top cell on Si cell, either with a 4-terminal or 2-terminal configuration, hold the current state of art efficiencies with 35.9% [5] and 33.3% [6], respectively.

Semiconductor NWs (NWs) have recently emerged as very promising candidates for a new generation of PV devices. The main advantage of NWs over thin films stems from the possibility to grow high structural quality NWs on mismatched substrates thanks to their small footprint that can accommodate the strain without creation of dislocations. NW solar cells have already been reported with efficiencies reaching 17.8% for InP [7], though for this proof-of-concept the NW array was fabricated by top-down lithography and dry etching of a InP substrate. Solar cells based on NW arrays grown by bottom-up techniques such as the vapor-liquid-solid (VLS) growth mechanism have reached efficiencies of 15.3% [8] for GaAs and 13.8% [9] for InP. Compared to the binary NWs studies reported above, ternary NWs offer more potential in term of band gap tuning. In particular, the energy gap of GaAsP NWs can be tuned to 1.7 eV, which provides the best theoretical efficiency for a III-V top cell on silicon tandem [10]. To date, only a few teams have reported experimental results on solar devices based on GaAsP NWs [11–14] and a certain number of epitaxial growth difficulties are still to be addressed [15–18].

Among others, the alloy homogeneity of ternary NWs is debated. Composition variations between different NWs grown in the same experiment [13,19] have been observed, as well as variations within a single NW along the growth axis [12,20,21]. Compositional changes have also been observed at the corners of the hexagonal cross-section of AlInP [22,23], AlGaAs [24,25], and GaAsP

[26,27] core-shell NWs. These features have been linked to different diffusion lengths for the species during shell growth.

Beside segregation at the edges during radial growth, it is commonly reported that unintentional radial growth occurs concurrently to the VLS axial growth. This has been particularly investigated in binary III-V nanowires, for which the concurrent VLS and VS growth results in particular NW shapes [28–33]. For ternary III-V NWs, the unintentional radial growth creates a core-shell structure, in which the chemical composition of the shell often differs from that of the NW core, as reported for AlGaAs [34,35], InGaAs [36,37], InAsSb [38] or GaAsSb [39] NWs. In GaAsP NWs, alloy variations between the unintentional NW shell and the core were observed independently of the growth method, MOCVD [40] or MBE [21,27]. The presence of such unintentional shell with a different chemical composition compared to the NW core poses problems for the design and fabrication of NW-based optoelectronic devices.

For GaAsP nanowires, the presence of the unintentional shell and the factors that influence the composition mismatch between the core and the shell still need to be investigated. In this work, we study the unintentional shell that forms during the axial growth of self-catalyzed GaAsP NWs by using specific growth designs with well-controlled alloy compositions. We accurately measure the core and shell alloy compositions and we estimate the shell thickness using high angle annular dark field (HAADF) imaging and energy dispersive X-ray (EDX) chemical contrast. We also show how the substrate temperature can be used to limit the compositional difference between the NW core and shell.

3 Method

GaAsP NW ordered arrays were grown on boron-doped Si(111) substrates (resistivity 0.01-0.02 Ohm.cm, from Siltronix) using a patterned silica mask to localize the NW growth. A 25 nm thick silica layer was deposited by PECVD on fully deoxidized Si surfaces (HF 5% for at least 1 min, until the surface is hydrophobic). The silica mask was patterned with a hexagonal array of holes (pitch 500 nm) by electron beam lithography (Vistec EBPG 5000+, 100 KV) using a PMMA resist (495PMMA, 2%). Reactive ion etching based on SF_6/CHF_3 gasses was used to transfer the pattern into the silica mask. The sample was then cleaned successively in trichloroethylene, acetone and isopropanol. An oxygen plasma was used to remove organic contaminations. Before the introduction of the sample in the MBE load-lock, a HF treatment (HF 1%, 30s) was performed to fully expose the Si(111) surface at the bottom of the holes in the silica mask.

The patterned substrates were then outgazed at 500°C in the MBE system (RIBER 32) until the pressure reading reduces below 10^{-9} torr. The GaAsP NW growth was performed with elementary sources, using Ga as the VLS catalyst, in the so-called self-catalyzed growth mode. Gallium, Arsenic and Phosphorous were respectively provided using a standard effusion cell, a valved cracker source producing As_4 tetramers (cracker temperature 600°C) and a valved cracker source producing P_2 dimers (cracker temperature 900°C).

The substrate temperature was monitored by a pyrometer (IRCON 0.9micron) and maintained constant during the NW growth. Depending on the experiment the substrate temperature was fixed between 590°C and 620°C.

All elementary fluxes, including group V, were calibrated atomically using RHEED oscillations on GaAs(100) or GaP(100) surfaces (see references [41,42]). The Ga flux was maintained constant at the equivalent growth rate of 0.16 or 0.18 $nm.s^{-1}$.The As and P fluxes were varied so that the atomic flux (As+P):Ga value is between 1.5 and 1.8. The growth was started by opening the Ga shutter only

(between 30 sec and 60 sec) at the growth temperature to deposit selectively a liquid Ga droplet in each silica hole. Then the group V shutters were opened to grow the GaAsP NWs. The Ga cell temperature was the same for the pre-deposition step and the NW growth. The growth is terminated by closing all shutters and valves abruptly, and turning off the oven for a rapid cooling.

After the growth, the NWs were dispersed on copper grids and characterized by transmission electron microscopy (TEM) in a FEI Titan THEMIS tool operating at 200kV. During the scanning transmission electron microscopy (STEM) observations, bright field (BF) and high angle annular dark field (HAADF) images were collected to complement the energy dispersive X-ray spectroscopy (EDXS) chemical analysis acquired using a Brucker Super X detector. Conventional dark field TEM was used to highlight the possible twinning in the NW by selecting a single diffraction spot specific to one of the crystalline orientations.

4 Results

To experimentally evidence the formation of the unintentional shell during the growth of ternary GaAsP NWs we devise a dedicated growth sequence, which alternates three segments of different atomic composition. For this experiment, the substrate temperature was fixed to 600°C. Figure 1(b) shows this specific growth sequence, which starts with a pure GaP segment (approximately 1 µm long), continues with a $GaAs_{1-x}P_x$ segment with x≈0.5 (approximately 2 µm long) and finishes with a $GaAs_{1-x}P_x$ segment with x≈0.2 (approximately 2 µm long). These approximative alloy compositions correspond to experimental atomic flux ratios ε_P = P/(As+P) of ε_P =1, ε_P = 0.56 and ε_P = 0.18, respectively. The actual alloy composition of each NW segment will be investigated in detail in the following sections.

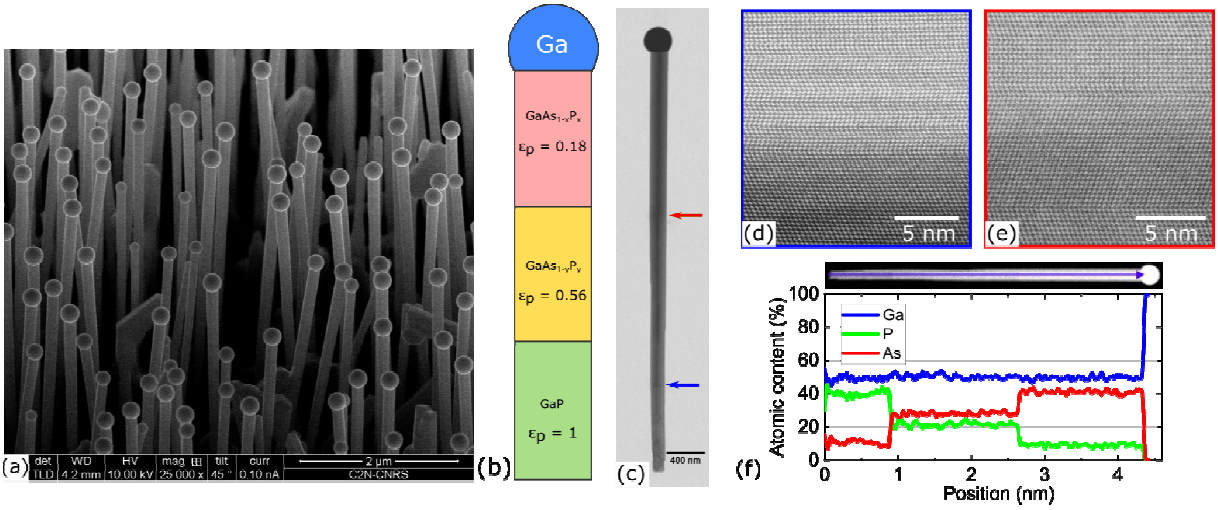

Figure 1: (a) SEM micrograph of the GaAsP NW array. (b) Scheme of the nominal structure of the GaAsP NW, showing the three alloy compositions (not to scale). (c) STEM-BF image of the grown NW viewed along the <110> zone-axis. (d), (e) High resolution STEM-HAADF images of the lower and upper heterostructures, showing twin defects and contrast changes due to composition variations. (f) Chemical composition profile of the NW along the growth direction obtained by using a STEM-EDX linescan.

Figure 1(a) shows the obtained NW array. The overall yield of vertical nanowires is about 50%. The wires are reverse-tapered from 140nm in diameter to 180 nm, 5 µm long and terminated by a Ga droplet. Most NWs are tilted due to strain from the shell heterostructures. They show no kink or specific defect between the three segments by SEM. Representative 5 µm long NWs were selected

for TEM studies. Using STEM-HAADF, figure 1(c), we can clearly distinguish each of the three segments. Figures 1(d) and 1(e) detail the lower, ε_P= 1 → 0.56, and the upper, ε_P=0.56 → 0.18 heterostructures, respectively. The crystal phase of the NWs is zinc-blende (cubic) with a large number of twins, independently of the alloy composition. The sharp contrast variations in each of the TEM images, Figures 1(d) and 1(e), demonstrate that the transition regions between two segments are only couple of monolayers thick. This fact indicates that the flux transients in the group V cells are relatively well controlled, even without employing specific flux switching methods like Priante *et al.* [43].

A simple EDX analysis using a line scan along the NW axis, figure 1(f), reveals the expected structure: three segments of distinct chemical compositions with increasing As content from bottom to tip. However, the reported composition values are rather unexpected: the bottom segment, nominally pure GaP (see Figure 1(b)), appears here as $GaAs_{1-x}P_x$ with x ≈ 0.8. This clearly demonstrates that the simplistic scheme of Figure 1(b) does not capture the actual structure of the NW.

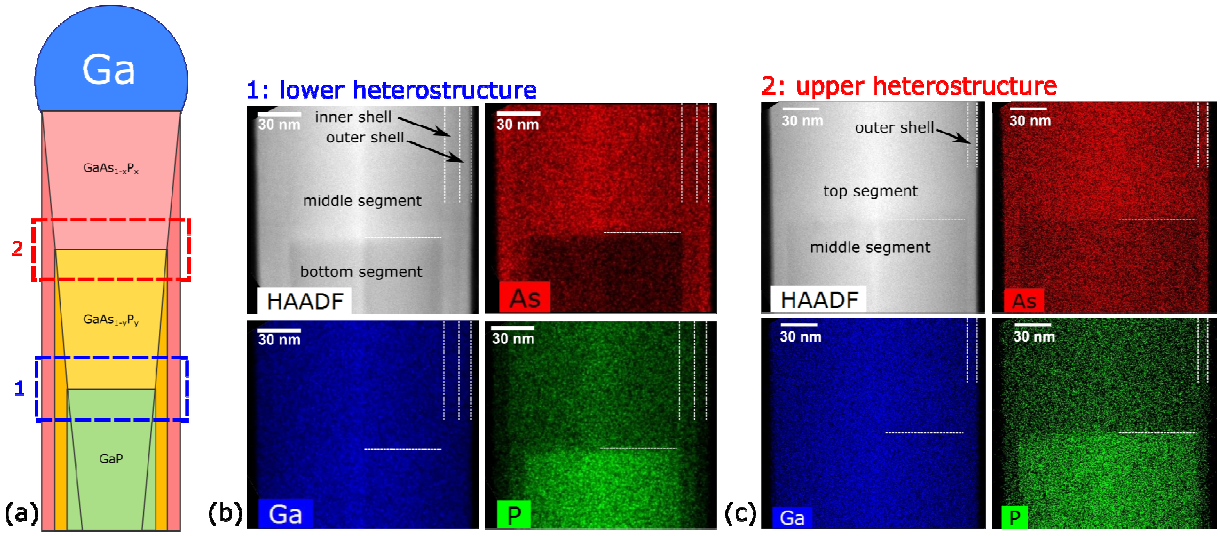

<u>Figure 2:</u> (a) Updated scheme the NW structure, including the radial and axial volumes created at each growth step, which results in a core-multishell structure, depending on the axial position along the wire. (b-c) TEM HAADF and EDX maps acquired along the <112> zone-axis, which reveal a double (b) and simple (c) core-shell structures at the lower and upper heterostructure, respectively. The observed shells are always As-rich (P-poor) compared to the NW core.

In Figure 2(a), we propose an improved schematic of the NW structure, in which the axial and radial growth modes have been taken into account to represent the actual alloy composition and material volume created at each growth step. The first segment only consists in binary GaP (ε_P =1), as the volumes created by the axial and radial growth are of the same composition (light green color). The next growth step (ε_P = 0.56) results in the expected $GaAs_{1-x}P_x$ segment by axial growth (yellow) while a $GaAs_{1-x}P_x$ shell is also grown radially (orange). In the final growth step (ε_P = 0.18) the last NW segment is formed by axial growth (light red) together with an additional shell (dark red). Note that the chemical compositions of the NW core and shell grown in same nominal conditions can differ due to the distinct growth mechanisms and flux geometries.

Figure 2(b) shows a high-resolution chemical map of the lower heterostructure (ε_P= 1 → 0.56) and the corresponding HAADF image acquired along a <112> zone axis. This specific orientation provides superior details when investigating the possible presence of a NW shell, as it will be discussed later. The Ga elementary map is uniform, as expected, but the As and P composition maps reveal the

presence of a As rich (or P poor) $GaAs_{1-x}P_x$ shell (≈ 20nm thick) around the NW core, irrespectively of the axial position of the heterostructure. Detailed analysis reveals that this As rich shell actually separates into two $GaAs_{1-x}P_x$ layers, the inner (x≈0.4) and outer shells (x≈0.2) with a larger As content in the outer shell, see white lines on the figure 2(b). Precise quantifications of the alloy compositions will be presented later in the discussion section.

Figure 2(c) presents the detailed analysis of the upper heterostructure, ε_P=0.56 → 0.18. Similarly to the lower heterostructure, the Ga map is uniform while the As and P map show opposite variations. Here we observe an As rich shell, approximate composition $GaAs_{1-x}P_x$ with x≈0.2, wrapped all around the heterostructure in the NW core.

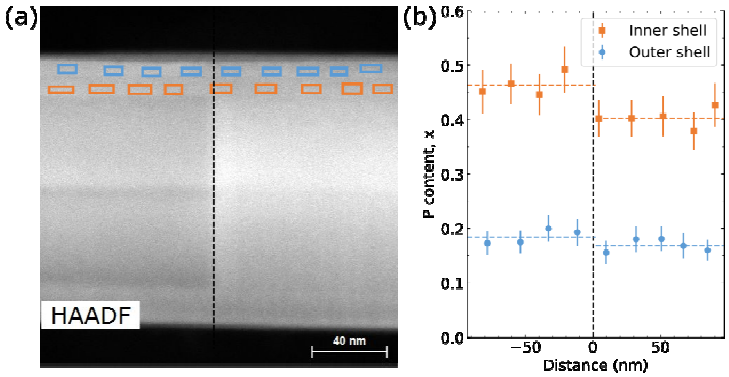

Figure 3: (a) Detailed analysis of the lower heterostructure by STEM-HAADF (<112> zone axis). The marked areas are used for the determination by EDX of locally averaged compositions. (b) Composition profile of the outer and inner shells with respect to the distance to the heterostructure. Dashed lines are the average compositions to the left and to right of the heterostructure.

In Figure 3, we show a detailed chemical analysis of the lower heterostructure shown in Figure 2(b). We focus here on the chemical composition of each shell, inner (orange color) and outer (blue color), across the heterostructure in the NW core. The shells are regularly sampled using rectangular areas to obtain a local averaged EDXS chemical composition, see Figure 3(a). Figure 3(b) shows the obtained composition against their position *d* relative to the core heterostructure. For both shells we observe a slight decrease of the P content, or an increase of the As, as we move from the lower GaP core (*d*<0) to the next GaAsP NW core (*d*>0).

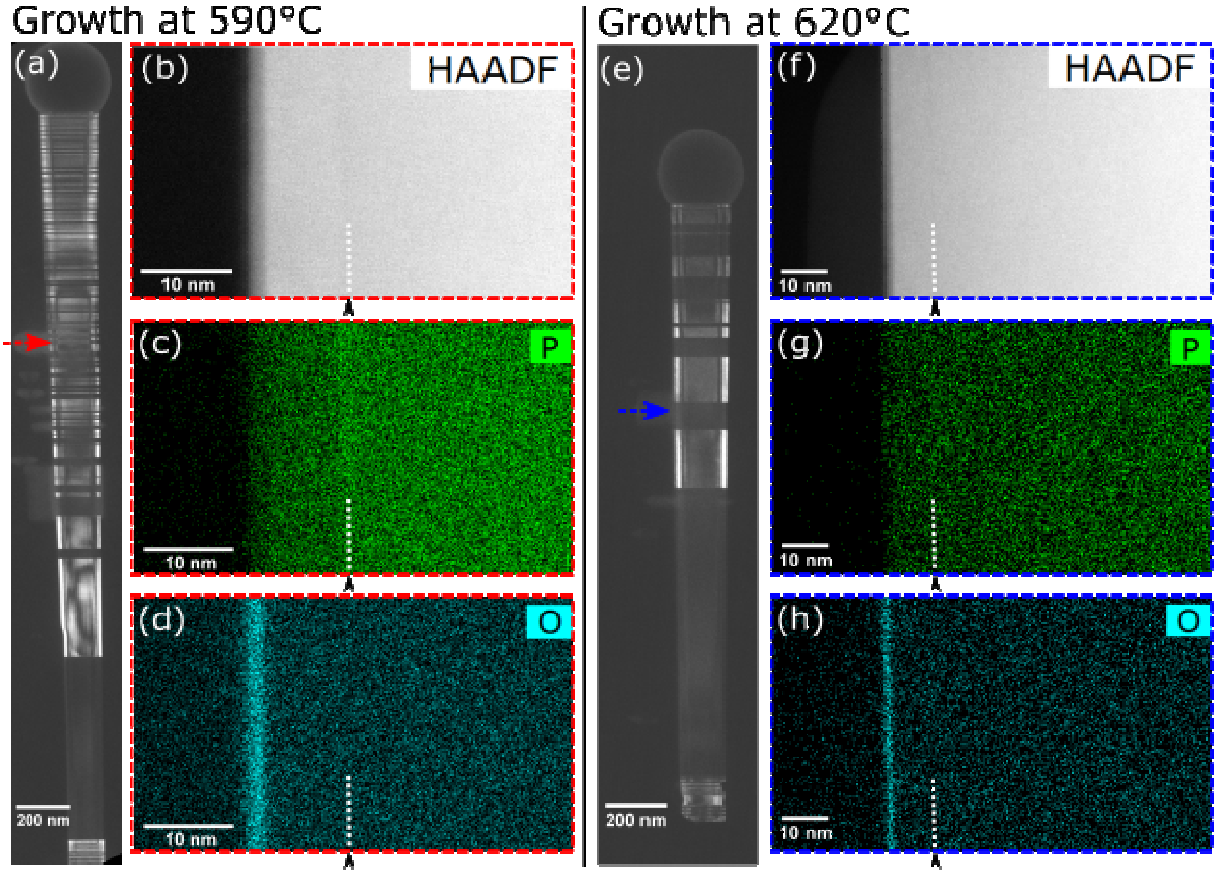

Figure 4: Comparison between NWs grown at 590°C (a-d) and 620°C (e-h), respectively. (a)(e) TEM-DF micrographs along the <110> zone-axis, highlighting one of the twins in the ZB structure. The red and blue arrows indicate zones further analyzed by EDX. (b-d) Details of the NW shell grown at 590°C, observed by STEM-HAADF (b) and EDX showing the corresponding P and O chemical maps (c,d). The white dotted line marks the interface between the As-rich (P-poor) shell and the NW core. (e-h) Similar analysis for the NW grown at 620°C, with no visible change in the chemical composition between core and shell.

The observed small variations of the chemical composition in the NW shell with that of the NW core suggest that the shell alloy content may be influenced by other factors than the elementary fluxes impinging the NW sidewalls. In Figure 4, we investigate the effect of the substrate temperature on the NW structure and chemical composition. Here, two $GaAs_{1-x}P_x$ NWs (x≈ 0.2) are grown in a single step using the same group III (Ga at the equivalent growth rate of 0.18 $nm.s^{-1}$) and V flux (ε_P= 0.24, (As+P)/Ga = 1.5). The first sample, Figure 4(a-d), is grown at 590°C, while the second sample, Figure 4(e-h), is grown using a higher substrate temperature, 620°C. To account for the axial growth speed reduction with temperature, the growth duration was increased from 20 min to 40 min. The two experiments were performed in succession to minimize any experimental variation. Both NWs have comparable diameter (190 nm and 170 nm below the droplet). Using conventional TEM, Figure 4(a) and 4(e), we observe that they still differ in length (2800nm at 590°C and 2000 nm at 620°C) despite the change in growth duration. They both present a cubic structure with several twins, identified by the contrast change in the DF TEM images. In our growth conditions, the lower substrate temperature (590°C) leads to more defective structure, Figure 4(a), compared the higher growth temperature (620°C), Figure 4(e). Chemical analysis using STEM-EDX and HAADF (Figure 4(b-d) and 4(f-h)) is extracted from an area situated at approximately the same distance from the NW catalyst (respectively 800 nm and 700nm). We clearly observe the presence of an As rich (P poor) shell

around the NW core for the sample grown at 590°C, Figure 4(c), and we cannot distinguish any shell in the EDX map acquired in the same conditions for the sample grown at 620°C, Figure 4(g). Chemical maps of the O content, Figure 4(d) and Figure 4(h), confirm that the native oxide on the NW outer surface is limited to the first 2 nm and cannot be confused with the GaAsP shell.

Interestingly, the GaAsP shell is separated from the NW core by a dark line in HAADF for both samples, independently of the growth temperature; see dotted white line in Figure 4(b) and Figure 4(f). The chemical map of the sample grown at low temperature, Figure 4(c), shows that this dark HAADF contrast is associated to a P-rich region. This feature is not visible Figure 4(g) due to the low spatial resolution of this particular EDX map.

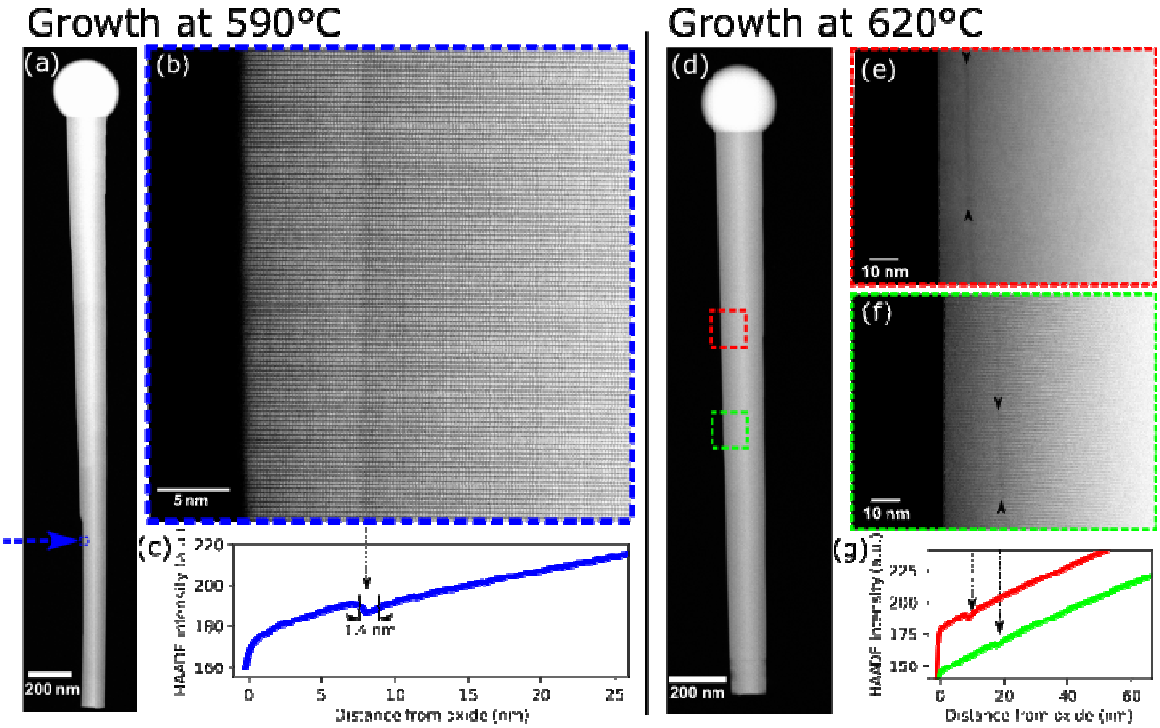

<u>Figure 5:</u> Details of the core-shell interface. (a) Overview of NW grown at 590°C using dark field TEM along the <112> zone-axis. (b) Atomically resolved STEM-HAADF of the NW shell at the location indicated by an arrow in (a). (c) Corresponding HAADF intensity profile. (d-g) Similar observations for the NW grown at 620°C. (e-f) Details of the shell observed by STEM-HAADF toward the NW top (red rectangle) and NW base (green rectangle). Black arrows mark the position of the dark line at the region used to compute the respective HAADF intensity profile in (g), toward the NW top (red line, offset) and NW base (green line).

To better characterize this P-rich interface, we have performed high resolution STEM-HAADF. The figure 5(a-b) presents the details of the core-shell interface of the NW grown at low temperature (590°C). We clearly distinguish the dark line between the NW core and shell. The HAADF intensity profile (Figure 5 (c)), reveals that the dark region is about 7 monolayers thick (1.4 nm).

Figures 5(d-f) show high resolution HAADF images of the NW grown at high temperature (620°C). The dark contrast is also well visible in Figures 5(e) and (f), which detail upper and lower parts of the NW, respectively. The corresponding HAADF profiles, Figure 5(g), reveal that the P-rich interface is close to the NW outer surface at the top of the NW and that it is buried below an increasingly thicker shell as we move toward the base of the NW.

5 Discussion

The presence of an unintentional shell of different composition than the NW core obfuscates the simple line scan analysis presented in Figure 1(f). The average composition must be carefully deconvolved using the actual hexagonal geometry, core diameter, shell thickness and shell composition to obtain the correct NW core composition (see Supplementary Information and [17]).

Table 1 summarizes the measured and corrected chemical compositions for the 3-segment GaAsP NW. Note that the corrected alloy composition of the first segment, x=1, now matches the experimental growth conditions, nominally pure GaP. At 600°C (Table 1), the unintentional shell grown is As rich, Δx = -0.03, independently of the P content in the NW core, x_{core}=0.44 or x_{core}=0.18. This difference is even higher for the sample grown at a lower temperature, 590°C (Table 2) with Δx = -0.09 using comparable group V fluxes.

Table 1: Core and shell compositions in the 3 segments of the $GaAs_{1-X}P_x$ NW presented in Figure 1 and 2, measured by STEM-EDX. The measurements were taken at the lower and upper heterostructure, as indicated in Figure 2. The suffix "-APP" refers to the apparent composition, whereas the suffix "-CORR" refers to the corrected composition, which accounts for the surrounding shell. $\Delta X_{CORE-SHELL}$ is the composition difference between the core and the shell formed during the same segment growth.

LOCATION	LOWER HETEROJUNCTION		UPPER HETEROJUNCTION	
SEGMENT	Bottom	Middle	Middle	Top
$X_{OUTER\ SHELL}$	**0.20 ± 0.01**	**0.16 ± 0.01**	**0.16 ± 0.01**	**0.14 ± 0.01**
$X_{INNER\ SHELL-APP}$	0.41 ± 0.02	0.36 ± 0.02	-	-
$X_{INNER\ SHELL-CORR}$	**0.47 ± 0.03**	**0.41 ± 0.03**	-	-
$X_{CORE-APP}$	0.75 ± 0.03	0.38 ± 0.02	0.40 ± 0.02	0.17 ± 0.01
$X_{CORE-CORR}$	**1 ± 0.04**	**0.44 ± 0.025**	**0.44 ± 0.03**	**0.18 ± 0.01**
$\Delta X_{CORE-SHELL}$	-	**0.03 ± 0.04**	-	**0.04 ± 0.02**

Table 2: Core and shell compositions of the $GaAs_{1-X}P_x$NWs grown at lower and higher temperature, as presented in Figure 4, measured by STEM-EDX. The measurements were taken at the zones indicated in Figure 4(a) and 4(e). The notation is the same as in table 1.

GROWTH TEMPERATURE	590°C	620°C
X_{SHELL}	**0.20 ± 0.01**	**0.235 ± 0.01**
$X_{CORE-APP}$	0.27 ± 0.01	0.24 ± 0.01
$X_{CORE-CORR}$	**0.29 ± 0.02**	**0.24 ± 0.02**
$\Delta X_{CORE-SHELL}$	**0.09 ± 0.02**	**0.005 ± 0.02**

Unintentional As-rich shells on MBE-grown GaAsP NWs have been observed on Au-catalyzed NWs [21] and Ga-catalyzed NWs [27]. In addition to the As-rich shell, a P-enrichment at the <112> corners of the shell was also reported by Himwas *et al.*[27] and Zhang *et al.* [26]. Following Mohseni *et al.* [21], the core-shell composition mismatch could be attributed to a P-enrichment of the core due to enhanced P adatom migration on the Si(111) surface towards the VLS catalyst. However other experimental studies have shown that group V diffusion is unlikely on the NW sidewall [42] and that the migration length of atoms on SiOx masks, as used here, is very small [33].

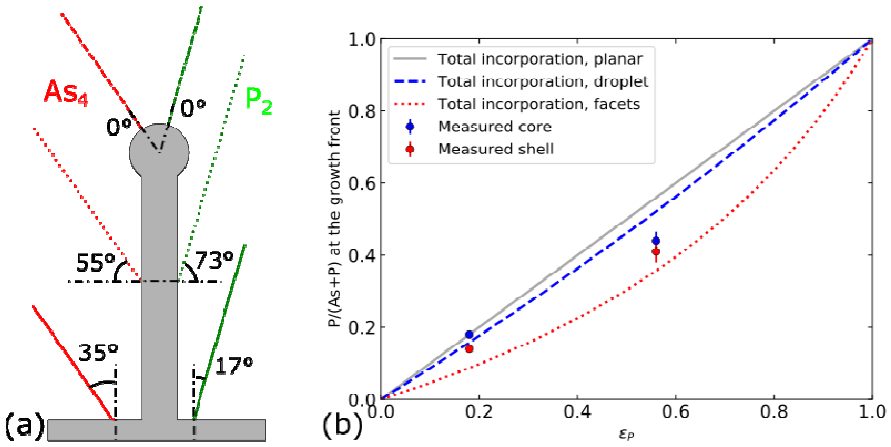

Figure 6: (a) Illustration of the different cell inclinations in our MBE chamber, leading to different effective fluxes on the droplet (dashed line), planar surface (filled line) and NW sidewalls (dotted lines). (b) Effective proportion of P atoms at the different growth fronts relative to the P proportion in the vapor phase, only considering directly impinging fluxes. Filled circles are our composition measurements by STEM-EDX at the upper and lower heterostructures.

In a first attempt to explain the different alloy contents between the NW core and shell, we first consider the geometry of the MBE chamber. Due to the different incident angles of the P and As cells in our MBE, the geometrical corrections for the direct fluxes impinging the droplet and the sidewalls differ slightly between As and P, see Figure 6(a). These simple corrections strictly depend on the local configuration of the MBE chamber. Assuming the total incorporation of the group V atoms, we plot in Figure 6(b) the P content in the different solids (NW core, sidewall or planar layers) as a function of the P content in the total group V flux, taking the planar surface as a reference. In our configuration, the local arrangement of the group V cells leads to a higher P content in the NW core (blue dashed line) than the shell (red dotted line), which loosely matches our experimental results (dots). However such a simplistic growth model, only based on directly impinging fluxes, is not accurate enough to make compositional predictions if the re-emitted fluxes and shadowing effects are not taken into account [33,44–46].

The relative P-to-As incorporation at the sidewall surface must also be considered. A preferred As incorporation relative to P was largely reported for GaAsP layers grown by solid-source MBE [47–52] or gas-source MBE [53,54]. The P content in the layer is found lower than the P content in the vapor phase for group III-limited growth, which is justified by kinetics arguments [50,51]. The local growth conditions at the NW sidewalls are not known, but as a Ga droplet only forms at the top of the wire we can propose a group III limited regime for the shell. In these conditions, the respective kinetics of P and As incorporation on (110) surfaces could also play an important role in the final composition.

Keeping geometrical corrections and all impinging fluxes constant, the local unintentional shell composition is found to depend on that of the NW core. Using Figure 3(b), we measure an averaged local content x = 0.46 on the inner shell grown on the GaP core (first segment), which rapidly decreases to x = 0.40 when grown on the GaAsP core (x_{core}=0.44, second segment). This observation could be related to a “lattice-pulling” effect, first reported and described by Stringfellow on GaInP [55]. Qualitatively, the epitaxy of a mismatched layer adds an elastic strain term to the total free energy. This tends to displace the solid composition to lower this elastic strain, which is balanced by the resulting increase in the chemical free energy. A precise quantification of this effect would necessitate to model the complete strain state in the present core-shell NWs [56], which is beyond the scope of this paper. However, we observe a qualitative match, as the local P composition of the

shell decreases with that of the NW core, at locations only separated by a few tens of nanometers, Figure 3(a).

In addition to strain-based effect, we measure a strong difference between the unintentional shell grown at low and high temperatures (Figure 4). Compositional variations of GaAsP with temperature have already been observed in planar GaAsP layers with conflicting results. The P content has been either found to decrease [48] or to increase with the substrate temperature [50]. The possible interpretations are that an increase of the growth temperature favors the evaporation of As from the substrate [50] or the sublimation of As precursor state on the growing surface [51], leading to larger P contents in the solid. However the actual growth rate, V/III ratio, and molecular form of the precursors can also play a role [51].

In the NW core, we observe a decrease of the phosphorus content from x = 0.29 at 590°C to x = 0.24 at 620°C. This variation occurs despite the use of identical fluxes and geometry. As the VLS growth is group V limited, it is very sensitive not only to the direct group V fluxes but also to the re-evaporation of group V species from the liquid droplet [57]. The final chemical composition of the material is obtained by balancing the impinging and re-evaporation fluxes of group V element in the liquid droplet. The actual balance depends on the thermodynamics parameters of each species and compound, which are different for As, P, GaAs and GaP [58]. Compared to planar layer growth, which typically operates in the group III limited growth regime, the VLS growth of the NW core operates in a distinct regime for which results extrapolated from planar layer studies may not be valid.

In our growth conditions, the composition of the VLS grown NW core (group V limited) shows a decreasing P content with temperature while the VS-grown shell (possibly group III limited) has an opposite variation. Therefore, there should exist a growth temperature for which the core and shell composition can be made equal. In our experiment, for a group V flux composition ε_P= 0.24, a substrate temperature of 620°C leads to a uniform composition x = 0.24 in the core and in the shell. One could perform this optimization for each group V flux composition, ε_P, by either lowering or increasing the substrate temperature depending on the initial starting point.

Even in the case of comparable alloy content in the NW core and shell at high temperature growth (620°C), we still observe a dark region by HAADF between the NW core and shell in Figure 5. The dark HAADF contrast suggests a higher P content, which is confirmed in the EDX analysis of Figure 4(c). The position of this local P-rich region correlates with that of the NW core-shell interface, which is buried below an increasingly thicker shell, Figure 5(e-g).

The analysis of the wire grown at high temperature (620°C) shows that the thin interface between the VS-grown shell and the VLS-grown core remains P-rich, even when the growth conditions have been adapted to match the core and shell chemical compositions. This P-rich material can only form just after or during the VLS growth of the top layer of the NW core, before the VS grown shell covers the NW sidewall. Although the exact origin of this P-rich interface is beyond the scope of this article, we can suggest a few alternatives. First, a very fast reaction of the exposed (110) facet with the vapor phase just after it is formed, i.e. P-enrichment after the VLS growth. Second, a local segregation of P at the triple phase line inside the Ga droplet, i.e. P-enrichment during the VLS growth. We note that some sort of segregation at the triple phase line has been reported in the nanowire literature [59,60] but limited to inhomogeneities in dopant concentrations, orders of magnitude below the compositional variations observed here.

6 Conclusion

We have unambiguously evidenced the formation of a shell during the VLS growth of self-catalyzed GaAsP nanowires by growing successive core alloy compositions. This unintentional shell is always present around the nanowires and results from the radial growth operating on the NW sidewall in the VS mode. The chemical composition of the shell is usually different from that of the NW core due to the distinct growth mechanisms. By adjusting the growth temperature, we find that it is possible to match the chemical composition of this unintentional GaAsP shell with the GaAsP core. Even in these favorable growth conditions, the interface between the NW core and shell still exhibits a local P-enrichment. While the later permits to precisely localize the position of the core shell interface in our GaAsP NWs, it is not clear how this P-rich region is formed. Yet the removal of such inhomogeneities is important for NW-based devices using ternary III-V semi-conductors.

7 Acknowledgements

This project has been supported by the French government in the frame of the “Programme d'Investissement d'Avenir” - ANR-IEED-002-01 and by the ANR projects Nanocell (ANR-15-CE05-0026) and Hetonan (ANR-15-CE05-0009). The TEM tool used in this study was funded by the project TEMPOS (ANR-10-EQPX-50).

8 References

[1] ISE @Fraunhofer 2018 Photovoltaics Report, updated: 27 August 2018

[2] Green M A, Hishikawa Y, Dunlop E D, Levi D H, Hohl-Ebinger J, Ho-Baillie A W H W Y, Warta W, Dunlop E D, Levi D H, Hohl-Ebinger J and Ho-Baillie A W H W Y 2018 Solar cell efficiency tables (version 52) *Prog. Photovoltaics Res. Appl.* **26** 427–36

[3] Richter A, Hermle M and Glunz S W 2013 Reassessment of the Limiting Efficiency for Crystalline Silicon Solar Cells *IEEE J. Photovoltaics* **3** 1184–91

[4] Feifel M, Ohlmann J, Benick J, Hermle M, Belz J, Beyer A, Volz K, Hannappel T, Bett A W, Lackner D and Dimroth F 2018 Direct Growth of III–V/Silicon Triple-Junction Solar Cells With 19.7% Efficiency *IEEE J. Photovoltaics* 1–6

[5] Essig S, Allebé C, Remo T, Geisz J F, Steiner M A, Horowitz K, Barraud L, Ward J S, Schnabel M, Descoeudres A, Young D L, Woodhouse M, Despeisse M, Ballif C and Tamboli A 2017 Raising the one-sun conversion efficiency of III–V/Si solar cells to 32.8% for two junctions and 35.9% for three junctions *Nat. Energy* **2** 17144

[6] Cariou R, Benick J, Feldmann F, Höhn O, Hauser H, Beutel P, Razek N, Wimplinger M, Bläsi B, Lackner D, Hermle M, Siefer G, Glunz S W, Bett A W and Dimroth F 2018 III–V-on-silicon solar cells reaching 33% photoconversion efficiency in two-terminal configuration *Nat. Energy* **3** 326–33

[7] van Dam D, van Hoof N J J, Cui Y, van Veldhoven P J, Bakkers E P A M, Gómez Rivas J and Haverkort J E M 2016 High-Efficiency Nanowire Solar Cells with Omnidirectionally Enhanced Absorption Due to Self-Aligned Indium–Tin–Oxide Mie Scatterers *ACS Nano* **10** 11414–9

[8] Aberg I, Vescovi G, Asoli D, Naseem U, Gilboy J P, Sundvall C, Dahlgren A, Svensson K E, Anttu N, Bjork M T and Samuelson L 2016 A GaAs Nanowire Array Solar Cell With 15.3% Efficiency at 1 Sun *IEEE J. Photovoltaics* **6** 185–90

[9] Wallentin J, Anttu N, Asoli D, Huffman M, Aberg I, Magnusson M H, Siefer G, Fuss-Kailuweit P, Dimroth F, Witzigmann B, Xu H Q, Samuelson L, Deppert K and Borgstrom M T 2013 InP

Nanowire Array Solar Cells Achieving 13.8% Efficiency by Exceeding the Ray Optics Limit *Science (80-.).* **339** 1057–60

[10] LaPierre R R 2011 Theoretical conversion efficiency of a two-junction III-V nanowire on Si solar cell *J. Appl. Phys.* **110** 014310

[11] Wu J, Li Y, Kubota J, Domen K, Aagesen M, Ward T, Sanchez A, Beanland R, Zhang Y, Tang M, Hatch S, Seeds A and Liu H 2014 Wafer-scale fabrication of self-catalyzed 1.7 eV GaAsP core-shell nanowire photocathode on silicon substrates *Nano Lett.* **14** 2013–8

[12] Holm J V, Jørgensen H I, Krogstrup P, Nygård J, Liu H and Aagesen M 2013 Surface-passivated GaAsP single-nanowire solar cells exceeding 10% efficiency grown on silicon *Nat. Commun.* **4** 1498

[13] Tchernycheva M, Rigutti L, Jacopin G, de Luna Bugallo A, Lavenus P, Julien F H, Timofeeva M, Bouravleuv A D, Cirlin G E, Dhaka V, Lipsanen H and Largeau L 2012 Photovoltaic properties of GaAsP core–shell nanowires on Si(001) substrate *Nanotechnology* **23** 265402

[14] Wood B 2017 *Fabrication and Characterization of GaAsP Nanowire-on-Silicon Tandem Photovoltaic Cells* (McMaster University)

[15] Zhang Y, Wu J, Aagesen M, Holm J, Hatch S, Tang M, Huo S and Liu H 2014 Self-Catalyzed Ternary Core–Shell GaAsP Nanowire Arrays Grown on Patterned Si Substrates by Molecular Beam Epitaxy *Nano Lett.* **14** 4542–7

[16] Zhang Y, Fonseka H A, Aagesen M, Gott J A, Sanchez A M, Wu J, Kim D, Jurczak P, Huo S and Liu H 2017 Growth of Pure Zinc-Blende GaAs(P) Core–Shell Nanowires with Highly Regular Morphology *Nano Lett.* **17** 4946–50

[17] Mohseni P K, Maunders C, Botton G A and LaPierre R R 2007 GaP/GaAsP/GaP core–multishell nanowire heterostructures on (111) silicon *Nanotechnology* **18** 445304

[18] Metaferia W, Persson A R, Mergenthaler K, Yang F, Zhang W, Yartsev A, Wallenberg R, Pistol M E, Deppert K, Samuelson L and Magnusson M H 2016 GaAsP Nanowires Grown by Aerotaxy *Nano Lett.* **16** 5701–7

[19] Zhang Y, Sanchez A M, Sun Y, Wu J, Aagesen M, Huo S, Kim D, Jurczak P, Xu X and Liu H 2016 Influence of Droplet Size on the Growth of Self-Catalyzed Ternary GaAsP Nanowires *Nano Lett.* **16** 1237–43

[20] Glas F, Harmand J-C and Patriarche G 2010 Nucleation Antibunching in Catalyst-Assisted Nanowire Growth *Phys. Rev. Lett.* **104** 135501

[21] Mohseni P K, Rodrigues A D, Galzerani J C, Pusep Y A and LaPierre R R 2009 Structural and optical analysis of GaAsP/GaP core-shell nanowires *J. Appl. Phys.* **106** 124306

[22] Sköld N, Wagner J B, Karlsson G, Hernán T, Seifert W, Pistol M-E and Samuelson L 2006 Phase Segregation in AlInP Shells on GaAs Nanowires *Nano Lett.* **6** 2743–7

[23] Wagner J B, Sköld N, Reine Wallenberg L and Samuelson L 2010 Growth and segregation of GaAs–AlxIn1−xP core-shell nanowires *J. Cryst. Growth* **312** 1755–60

[24] Rudolph D, Funk S, Döblinger M, Morkötter S, Hertenberger S, Schweickert L, Becker J, Matich S, Bichler M, Spirkoska D D, Zardo I, Finley J J, Abstreiter G and Koblmüller G 2013 Spontaneous alloy composition ordering in GaAs-AlGaAs core-shell nanowires *Nano Lett.* **13** 1522–7

[25] Mancini L, Fontana Y, Conesa-Boj S, Blum I, Vurpillot F, Francaviglia L, Russo-Averchi E, Heiss

M, Arbiol J, Morral A F i and Rigutti L 2014 Three-dimensional nanoscale study of Al segregation and quantum dot formation in GaAs/AlGaAs core-shell nanowires *Appl. Phys. Lett.* **105** 243106

[26] Zhang Y, Sanchez A M, Wu J, Aagesen M, Holm J V., Beanland R, Ward T and Liu H 2015 Polarity-driven quasi-3-fold composition symmetry of self-catalyzed III-V-V ternary core-shell nanowires *Nano Lett.* **15** 3128–33

[27] Himwas C, Collin S, Rale P, Chauvin N, Patriarche G, Oehler F, Julien F H, Travers L, Harmand J-C and Tchernycheva M 2017 In situ passivation of GaAsP nanowires *Nanotechnology* **28** 495707

[28] Küpers H, Lewis R B, Tahraoui A, Matalla M, Krüger O, Bastiman F, Riechert H and Geelhaar L 2018 Diameter evolution of selective area grown Ga-assisted GaAs nanowires *Nano Res.* **11** 2885–93

[29] Sartel C, Dheeraj D L, Jabeen F and Harmand J C 2010 Effect of arsenic species on the kinetics of GaAs nanowires growth by molecular beam epitaxy *J. Cryst. Growth* **312** 2073–7

[30] Colombo C, Spirkoska D, Frimmer M, Abstreiter G and Fontcuberta I Morral A 2008 Ga-assisted catalyst-free growth mechanism of GaAs nanowires by molecular beam epitaxy *Phys. Rev. B - Condens. Matter Mater. Phys.* **77** 2–6

[31] Gibson S and Lapierre R 2013 Study of radial growth in patterned self-catalyzed GaAs nanowire arrays by gas source molecular beam epitaxy *Phys. Status Solidi - Rapid Res. Lett.* **7** 845–9

[32] Munshi A M, Dheeraj D L, Fauske V T, Kim D C, Huh J, Reinertsen J F, Ahtapodov L, Lee K D, Heidari B, van Helvoort A T J, Fimland B O and Weman H 2014 Position-Controlled Uniform GaAs Nanowires on Silicon using Nanoimprint Lithography *Nano Lett.* **14** 960–6

[33] Oehler F, Cattoni A, Scaccabarozzi A, Patriarche G, Glas F and Harmand J-C 2018 Measuring and Modeling the Growth Dynamics of Self-Catalyzed GaP Nanowire Arrays *Nano Lett.* **18** 701–8

[34] Lim S K, Tambe M J, Brewster M M and Gradečak S 2008 Controlled growth of ternary alloy nanowires using metalorganic chemical vapor deposition *Nano Lett.* **8** 1386–92

[35] Chen C, Shehata S, Fradin C, LaPierre R, Couteau C and Weihs G 2007 Self-directed growth of AlGaAs core-shell nanowires for visible light applications *Nano Lett.* **7** 2584–9

[36] Guo Y N, Xu H Y, Auchterlonie G J, Burgess T, Joyce H J, Gao Q, Tan H H, Jagadish C, Shu H B, Chen X S, Lu W, Kim Y and Zou J 2013 Phase separation induced by Au catalysts in ternary InGaAs nanowires *Nano Lett.* **13** 643–50

[37] Mohseni P K, Behnam A, Wood J D, English C D, Lyding J W, Pop E and Li X 2013 In x Ga 1– x As Nanowire Growth on Graphene: van der Waals Epitaxy Induced Phase Segregation *Nano Lett.* **13** 1153–61

[38] Xu T, Dick K A, Plissard S, Nguyen T H, Makoudi Y, Berthe M, Nys J-P, Wallart X, Grandidier B and Caroff P 2012 Faceting, composition and crystal phase evolution in III–V antimonide nanowire heterostructures revealed by combining microscopy techniques *Nanotechnology* **23** 095702

[39] Conesa-Boj S, Kriegner D, Han X-L, Plissard S, Wallart X, Stangl J, Fontcuberta i Morral A and Caroff P 2014 Gold-Free Ternary III–V Antimonide Nanowire Arrays on Silicon: Twin-Free down to the First Bilayer *Nano Lett.* **14** 326–32

[40] Sun W, Huang Y, Guo Y, Liao Z M, Gao Q, Tan H H, Jagadish C, Liao X Z and Zou J 2015 Spontaneous formation of core-shell GaAsP nanowires and their enhanced electrical conductivity *J. Mater. Chem. C* **3** 1745–50

[41] Rudolph D, Hertenberger S, Bolte S, Paosangthong W, Spirkoska D, Döblinger M, Bichler M, Finley J J, Abstreiter G and Koblmüller G 2011 Direct observation of a noncatalytic growth regime for GaAs nanowires *Nano Lett.* **11** 3848–54

[42] Ramdani M R, Harmand J C, Glas F, Patriarche G and Travers L 2013 Arsenic pathways in self-catalyzed growth of GaAs nanowires *Cryst. Growth Des.* **13** 91–6

[43] Priante G, Patriarche G, Oehler F, Glas F and Harmand J C 2015 Abrupt GaP/GaAs Interfaces in Self-Catalyzed Nanowires *Nano Lett.* **15** 6036–41

[44] Gibson S J and LaPierre R R 2014 Model of patterned self-assisted nanowire growth *Nanotechnology* **25** 415304

[45] Kelrich A, Calahorra Y, Greenberg Y, Gavrilov A, Cohen S and Ritter D 2013 Shadowing and mask opening effects during selective-area vapor–liquid–solid growth of InP nanowires by metalorganic molecular beam epitaxy *Nanotechnology* **24** 475302

[46] Dalacu D, Kam A, Guy Austing D, Wu X, Lapointe J, Aers G C and Poole P J 2009 Selective-area vapour–liquid–solid growth of InP nanowires *Nanotechnology* **20** 395602

[47] Arthur J R and LePore J J 1969 GaAs, GaP, and GaAsxP1−x Epitaxial Films Grown by Molecular Beam Deposition *J. Vac. Sci. Technol.* **6** 545–8

[48] Matsushima Y and Gonda S 1976 Molecular Beam Epitaxy of GaP and GaAs(1-x)P(x) *Jpn. J. Appl. Phys.* **15** 2093–101

[49] Foxon C T, Joyce B A and Norris M T 1980 Composition effects in the growth of Ga(In)AsyP1-y alloys by MBE *J. Cryst. Growth* **49** 132–40

[50] Woodbridge K, Gowers J P and Joyce B A 1982 Structural properties and composition control of GaAsyP1−y grown by MBE on VPE GaAs0.63P0.37 substrates *J. Cryst. Growth* **60** 21–8

[51] Nomura T, Ogasawara H, Miyao M and Hagino M 1991 Composition control of GaAsP grown by molecular beam epitaxy *J. Cryst. Growth* **111** 61–4

[52] Shu-Dong W, Li-Wei G, Wen-Xin W, Zhi-Hua L, Ping-Juan N, Qi H and Jun-Ming Z 2005 Incorporation Behaviour of Arsenic and Phosphorus in GaAsP/GaAs Grown by Solid Source Molecular Beam Epitaxy with a GaP Decomposition Source *Chinese Phys. Lett.* **22** 960–2

[53] LaPierre R R, Robinson B J and Thompson D A 1996 Group V incorporation in InGaAsP grown on InP by gas source molecular beam epitaxy *J. Appl. Phys.* **79** 3021–7

[54] Hou H Q, Liang B W, Chin T P and Tu C W 1991 In situ determination of phosphorus composition in GaAs 1− x P x grown by gas-source molecular beam epitaxy *Appl. Phys. Lett.* **59** 292–4

[55] Stringfellow G B 1972 The importance of lattice mismatch in the growth of GaxIn1-xP epitaxial crystals *J. Appl. Phys.* **43** 3455–60

[56] Glas F 2015 *Strain in nanowires and nanowire heterostructures* vol 93

[57] Glas F, Ramdani M R, Patriarche G and Harmand J C 2013 Predictive modeling of self-catalyzed III-V nanowire growth *Phys. Rev. B - Condens. Matter Mater. Phys.* **88** 1–14

[58] Ansara I, Chatillon C, Lukas H L, Nishizawa T, Ohtani H, Ishida K, Hillert M, Sundman B, Argent

B B, Watson A, Chart T G and Anderson T 1994 A binary database for III–V compound semiconductor systems *Calphad* **18** 177–222

[59] Connell J G, Yoon K, Perea D E, Schwalbach E J, Voorhees P W and Lauhon L J 2013 Identification of an intrinsic source of doping inhomogeneity in vapor-liquid-solid-grown nanowires *Nano Lett.* **13** 199–206

[60] Hilse M, Ramsteiner M, Breuer S, Geelhaar L and Riechert H 2010 Incorporation of the dopants Si and Be into GaAs nanowires *Appl. Phys. Lett.* **96** 193104